Check for updates

Improved active fiber-based retroreflector with intensity stabilization and a polarization monitor for the near UV

VITALY WIRTHL,[1,*] LOTHAR MAISENBACHER,[1] JOHANNES WEITENBERG,[1,2] ALEXANDER HERTLEIN,[1] ALEXEY GRININ,[1] ARTHUR MATVEEV,[1,3] RANDOLF POHL,[4] THEODOR W. HÄNSCH,[1,3] AND THOMAS UDEM[1,3]

[1]*Max Planck Institute of Quantum Optics (MPQ), 85748 Garching, Germany*
[2]*RWTH Aachen University, 52062 Aachen, Germany*
[3]*Ludwig Maximilian University (LMU), 80539 Munich, Germany*
[4]*Johannes Gutenberg University, 55128 Mainz, Germany*
*vitaly.wirthl@mpq.mpg.de

Abstract: We present an improved active fiber-based retroreflector (AFR) providing high-quality wavefront-retracing anti-parallel laser beams in the near UV. We use our improved AFR for first-order Doppler-shift suppression in precision spectroscopy of atomic hydrogen, but our setup can be adapted to other applications where wavefront-retracing beams with defined laser polarization are important. We demonstrate how weak aberrations produced by the fiber collimator may remain unobserved in the intensity of the collimated beam but limit the performance of the AFR. Our general results on characterizing these aberrations with a caustic measurement can be applied to any system where a collimated high-quality laser beam is required. Extending the collimator design process by wave optics propagation tools, we achieved a four-lens collimator for the wavelength range 380–486 nm with the beam quality factor of $M^2 \simeq 1.02$, limited only by the not exactly Gaussian beam profile from the single-mode fiber. Furthermore, we implemented precise fiber-collimator alignment and improved the collimation control by combining a precision motor with a piezo actuator. Moreover, we stabilized the intensity of the wavefront-retracing beams and added in-situ monitoring of polarization from polarimetry of the retroreflected light.

1. Introduction

In the field of atomic, molecular and optical physics, different applications may require a high-quality laser beam, for instance fluorescence microscopy [1], single atom imaging [2], cold atom experiments [3], and quantum information research [4]. Some experiments, for instance in atom interferometry [5–7] or precision spectroscopy [8–10], depend upon a retroreflection of high-quality beams to create wavefront-retracing beams (also called phase-retracing beams [11]). For this purpose, we have constructed an active fiber-based retroreflector (AFR) that employs a beam emerging from a single-mode fiber that is collimated and coupled back into the same fiber with a highly reflective mirror. By maximizing the backcoupled light fraction, a wavefront-retracing standing wave of high quality is obtained whose performance critically depends on minimizing aberrations [11]. Creating such a beam is especially challenging in the far blue and near UV regions, owing to the increased sensitivity to lens surface imperfections as well as a limited number of suitable glasses and therefore lack of aberration-reduced composite elements such as achromatic doublets [12].

As an alternative approach to the AFR, optical cavities may provide wavefront-retracing beams, acting naturally as a filter of beam imperfections [13,14]. Our experiment requires a relatively low intra-cavity power of $< 30\ \mu W$ and thus small impinging power for a high finesse cavity.

The small impinging power would yield a noisy error signal for stabilizing the cavity length. Moreover, we need a large beam radius of $W_0 \sim 2$ mm, which may require to operate the cavity close to the stability edge or to use special cavity geometries [15,16]. Therefore, we rather chose to improve our existing AFR setup.

We use our AFR to suppress the first-order Doppler shift of one-photon transitions in atomic hydrogen from the metastable 2S level to nP levels. The first-order Doppler shift $\Delta\nu_D$ of a single atom with velocity $\vec{V}$ interacting with a wave described by a local wave vector $\vec{k}$ is given by

$$\Delta\nu_D = \vec{k} \cdot \vec{V}/2\pi = V\cos(\alpha)/\lambda, \tag{1}$$

where λ denotes the wavelength, V the magnitude of the atom's velocity vector and α its angle with respect to the wave vector. Cooling the atoms and aligning the angle α as good as possible to 90° reduces the Doppler shift. In our setup, for liquid-helium cooled atoms and our accuracy goal of $\lesssim 1$ kHz, the angle deviation $\delta\alpha$ from the perpendicular case ($\alpha = 90° + \delta\alpha$) would have to be less than $\delta\alpha < 1$ μrad. Apart from being mechanically challenging, in our setup such an alignment cannot be achieved due to the much larger laser and atomic beam divergence angles. Therefore, we further suppress the Doppler shift using two locally counter-propagating waves with wave vectors $+\vec{k}$ and $-\vec{k}$. The two beams need to be wavefront-retracing everywhere along the atomic beam trajectory, and the intensities of both beams have to be equal everywhere. The AFR helps to satisfy both conditions.

The previous setup [11] was successfully used to measure the 2S-4P transition in hydrogen at a wavelength of 486 nm. 2S-nP transitions in hydrogen with $n > 4$ bear the potential for an even higher precision and an improved determination of the Rydberg constant and proton radius due to their narrower natural linewidth [17]. To this end, we rebuilt our apparatus for the shorter wavelength of 410 nm (2S-6P transition) and have a laser system for 380–390 nm (2S-8P and higher) ready to be integrated into the apparatus for future measurements. Our improved setup is outlined in Sec. 2.

In the process of rebuilding the setup for shorter wavelength, an extended investigation of residual aberrations is necessary to achieve the required level of Doppler-shift suppression in the AFR. In our previous setup, aberrations were observed in the intensity of the collimated beam and ray tracing techniques alone were used to design the collimator [11]. This work demonstrates how weak aberrations may be overlooked in the collimated intensity beam profile, but revealed through characterization using the caustic measurement. We provide a theoretical description explaining how aberrations are characterized by observing intensity profiles in the caustic measurement. The collimator design procedure is extended by simulations using wave optics propagation, achieving a four-lens design with minimized aberrations such that the measured beam quality is only limited by the not exactly Gaussian beam profile of the single-mode fiber. The collimator, including the characterization of aberrations and the design process, is discussed in detail in Sec. 3.

In addition to the careful study of aberrations along with a novel collimator for the near UV, we present other significant improvements in the AFR. We added a piezo actuator to the precision motor for a more accurate adjustment of the distance between the fiber tip and the collimator which is crucial to optimize the retroreflection, as detailed in Sec. 4. Another improvement of our setup is the implementation of an intensity stabilization of the wavefront-retracing beams in the AFR, discussed in Sec. 5. Moreover, to deduce the in-situ polarization in the AFR, the polarization of the backcoupled light is continuously monitored. More information on polarimetry is given in Sec. 6. In Sec. 7 we summarize our results and give a brief outlook.

2. Active fiber-based retroreflector setup

The general concept of an active fiber-based retroreflector (AFR) is discussed in detail in a previous publication [11]. The main idea is to collimate a laser beam from a single-mode fiber

and use a highly reflective (HR) mirror to couple the light back through the collimator into the same fiber. Using a beamsplitter before the fiber, the backcoupled light fraction can be monitored and maximized by adjusting the distance between the collimator and the fiber, as well as the tip-tilt alignment of the HR mirror. This tip-tilt alignment is actively stabilized with piezoelectric actuators on the mirror mount [18]. Maximizing the backcoupled light fraction corresponds to optimizing the wavefront-retracing property of the beam: for a perfectly flat, fully reflective HR mirror and an aberration-free beam, the wavefront-retracing and amplitude matching conditions are satisfied if the waist of the collimated beam is located on the mirror, resulting in all of the optical power being coupled back into the fiber.

The optical setup of our hydrogen spectrometer relevant to the AFR is shown in Fig. 1. We start with around 100 mW of 410 nm laser light which is sent to the experiment through an 11 m-long polarization-maintaining (PM) fiber. An acousto-optic modulator (AOM) is used to scan the optical frequency across the resonance. An electro-optic modulator (EOM 1), in sequence with a polarizing beamsplitter (PBS) and half-wave plates, is used for intensity control. The light is transferred via another 5 m-long PM fiber to a polarization switching and polarimetry unit (PSPU). The intensity after this fiber is stabilized using the signal of photodetector PD 1 in combination with EOM 1 as an actuator (1st intensity stabilization). Additional photodetectors (PD 2, PD 3, and PD 4) monitor the intensity out-of-loop. In the PSPU, Glan-Thompson polarizers providing PER > 50 dB improve the polarization extinction ratio PER = P_{max}/P_{min} of light coupled into the last fiber, where P_{max} and P_{min} are the maximal and minimal transmitted optical powers in the two orthogonal polarization directions. Isolators in each arm suppress optical etalons, with lowest number of optical surfaces as possible placed after the isolators. The beam path of the unused polarization is blocked by the backside of the polarimeter which is used to measure the polarization of the returning light. In order to switch between horizontal and vertical linear polarizations, this polarimeter is manually moved to the other arm of the PSPU. After the PSPU, the light passes a non-polarizing beamsplitter (BS 2) and is sent through another beamsplitter (BS 3).
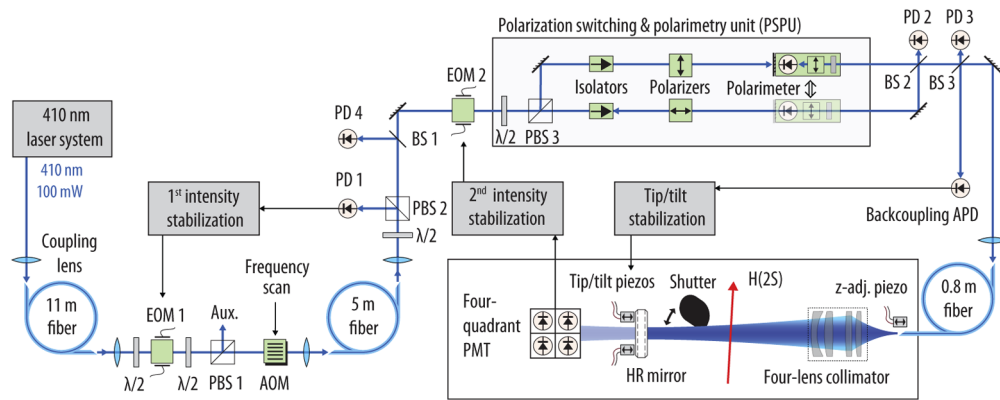
Fig. 1. Optical setup of the 2S-*n*P hydrogen apparatus relevant to the AFR. EOM: electro-optic modulator, $\lambda/2$: half-wave plate, PBS: polarizing beamsplitter, BS: non-polarizing beamsplitter, AOM: acousto-optic modulator, PD: photodetector, APD: avalanche photodiode, H(2S): metastable hydrogen atoms in the 2S level, PMT: photomultiplier tube, z-adj. piezo: adjustment of the fiber-collimator distance, HR mirror: highly reflective mirror. A polarimeter is placed into the unused arm of the PSPU to analyze the polarization of the returning light, whereas the part of the returning light in the used arm of the PSPU ends in the isolator.

Finally, the laser light (5-30 µW laser power) reaches the in-vacuum AFR setup via the last 80 cm-long polarization-maintaining (PM) fiber [19], see also Fig. 2 for an engineering drawing. The whole in-vacuum AFR setup is mounted on a rotatable cylinder (RC), which sits on ball bearings such that the angle between the spectroscopy laser beam (SB) and the metastable atomic hydrogen beam (H(2S) / AB) collinear to the 1S-2S preparation laser beam (PB) can be aligned close to 90°. The four-lens collimator (SC) is mounted onto a mirror mount combined with a manual precision rotation stage (RM, Thorlabs POLARIS-K2S3, PRM2/M). The collimation is adjusted with the help of a commercial fiber translation mount (Thorlabs SM1Z) which we rebuilt for accurate distance control using a precision motor (ZM, Newport 8301-V) combined with a piezo actuator (z-adj. piezo / ZP, Thorlabs PK4FQP2). This part is placed onto a cage system mounted to a flexure adjustment plate (CA, Thorlabs CP1XY) needed for precise centering between the fiber and the collimator, see Sec. 3.4. The light is retro-reflected by the HR mirror (custom-order from Layertec, reflectivity $R_{HR} > 99.995$ %, transmission $T \simeq 2 \times 10^{-5}$, substrate with $\lambda/30$ @ 633 nm irregularity and < 1.5 Å RMS roughness) and passes back through the fiber, where approximately one-half of the backcoupled light is detected after BS 3 on the avalanche photodiode (backcoupling APD) whose signal is used for the tip-tilt stabilization using piezo actuators (only the horizontal piezo actuator HP is shown in Fig. 2). Another fraction of the backcoupled light is split by BS 2, with the light then terminating either in the polarimeter or the isolator. The home-built remotely controlled shutter (SH) makes it possible to block the reflected beam for a measurement of the Doppler shifted spectroscopy signal.
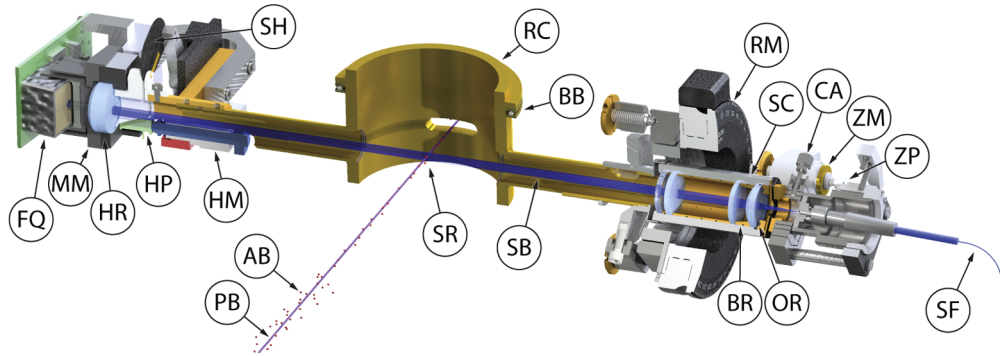
Fig. 2. 3D engineering drawing of the AFR assembly in vacuum for the 2S-6P hydrogen experiment. (AB) hydrogen atomic beam, (BB) base cylinder ball bearing, (BR) brass ring spacer between collimator lenses, (CA) collimator-fiber alignment, (FQ) four-quadrant photomultiplier, (HM) horizontal (tip) precision motor with (HP) piezo actuator of the (HR) highly reflective (MM) mirror mount, (OR) retainer with O-ring holding collimator lens system in place, (PB) 1S-2S preparation laser beam, (RC) rotatable base cylinder, (RM) collimator rotation mount, (SB) 410 nm spectroscopy laser beam, (SC) four-lens collimator, (SF) polarization-maintaining fiber, (SH) shutter, (SR) hydrogen 2S-6P transition spectroscopy region, (ZM) precision motor and (ZP) piezo actuator for fiber-collimator distance adjustment.

The sum signal of the four-quadrant photomultiplier (PMT/FQ, Hamamatsu R11265-200-M4) after the HR mirror is used for intensity stabilization of the wavefront-retracing beam, with EOM 2 serving as actuator (2nd intensity stabilization). The PMT is mounted under an angle of $\sim 10°$ with an interference bandpass filter (Edmund Optics 34-494, 10 nm-wide passband (FWHM), centered at 413 nm) and scattering disk (DG10-1500-A). The use of a position-sensitive

PMT has the practical advantage of misalignment monitoring. An angular misalignment of the HR mirror or the collimator-fiber system by 200 µrad leads to a complete loss of the backcoupled signal [11]. If the optimal orientation of AFR is lost (e.g., during work on the apparatus), the horizontal and vertical position signals of the PMT help to retrieve the alignment.

3.   Collimator with minimized aberrations in the near UV

In the AFR, the collimator plays a central role since aberrations may be imprinted on the wavefronts of the spectroscopy laser beams. These aberrations distort the wavefronts such that there may be no position in the collimated beam with a plane wavefront, and thus the backward-traveling beam will not retrace the wavefronts of the forward-traveling beam. The backcoupled light fraction is a quantity which characterizes how well the wavefront-retracing property is maintained, because this quantity is directly linked to the overlap integral of the forward- and backward-traveling beams. In our previous setup of the AFR at 486 nm, a collimator design based on two achromatic lens doublets was used to minimize aberrations and achieve a backcoupled fraction consistent with 100 % within 1 % [11]. Apart from correcting chromatic aberrations, which are irrelevant for our single-wavelength application, achromatic lens doublets have the advantage of reducing spherical aberration compared to a single lens, due to the fact that there are more refractive surfaces.

   With shorter wavelengths, designing and manufacturing suitable optics becomes more challenging since fewer glass types are sufficiently transparent. We chose to work with fused silica which has a high UV transmission down to 180 nm. In theory, aberration-free collimation can be achieved with a single aspheric lens of the desired shape. To this end, we tested custom-made aspheres [20] machined with the advanced technique of magnetorheological finishing (MRF) [21–23]. Unfortunately, imperfections due to mid-spatial frequency errors were still clearly visible on the collimated beam and only around 80 % of backcoupled light fraction could be achieved. Therefore, we chose to only work with spherical lenses which are available with small surface roughness.

   First, at 410 nm we tested a three-lens collimator based on spherical lenses. A design with minimized aberrations was found by following conventional ray-tracing techniques such as optimizing the point-spread function and minimizing the optical path difference of rays, similar to the previous two-achromats design at 486 nm [11]. However, when testing the assembled custom-made collimator we found that residual spherical aberrations limit the backcoupled fraction to 94.0(1.2) %. Contrary to our previous experience where collimator imperfections were clearly visible as distortions in the collimated beam [11], aberrations of the three-lens collimator were not visible in the intensity profiles of the collimated beam and were revealed only by a caustic measurement, i.e. beam profile measurements at different position within a caustic. For our application, the usual ray tracing design process was extended by wave optics propagation tools. Finally, together with the manufacturing company [24] we arrived at a four-lens design whose optical performance was confirmed with a caustic measurement and showed no aberrations above our detection limit. With this collimator, we achieved a measured backcoupled light fraction of 99.3(1.2) %, consistent with 100 %. In the following we describe the design and characterization process.

3.1.   Characterization of aberrations: caustic measurement

In the previous setup at 486 nm, imperfections of various collimators were identified by observing distortions in the intensity profiles of the collimated beam [11]. With the three-lens collimator designed for 410 nm, we do not observe any distortions in the collimated beam even after propagation of several meters. However, because of the 6 % missing backcoupled light fraction we know that the forward- and backward-traveling beams are not fully wavefront-retracing. Aberrations may solely be imprinted on the phase of electric field and remain imperceptible in

the intensity profile within a certain propagation range. Inspecting only the collimated beam after the collimator even up to arbitrarily large propagation distances, the corresponding aberrations may not appear as intensity distortions because only half of the caustic is accessible. Hence, aberrations present in the phase need to be transformed into distinct intensity distortions by propagation through the full caustic [25]. In principle, one could reveal the same information from wavefront sensors. Though more sophisticated wavefront measurement techniques are available [26–28], the commercial Shack-Hartmann wavefront sensor available to us was not accurate enough for this purpose (specified wavefront measurement accuracy of $\lambda/60$ RMS at 633 nm).
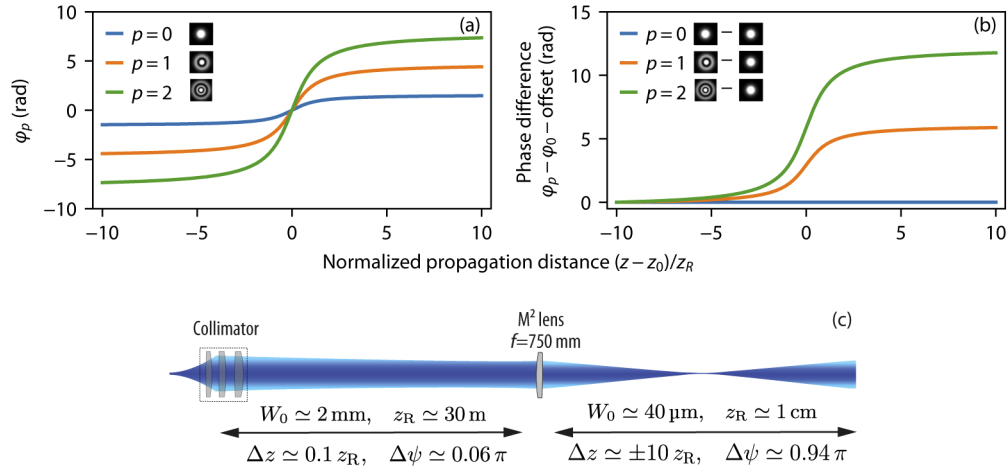
Fig. 3. (a) Mode-dependent phase φ_p according to Eq. (6) for the first three LG_p^0 modes with $p = 0, 1, 2$ over the normalized propagation distance $(z - z_0)/z_R$. (b) The phase difference between the modes is given by the Gouy phase, $\varphi_p - \varphi_0 = 2p\,\psi$, and determines how aberrations present in the phase transform into intensity. The constant phase offset between the modes has been subtracted such that at the point where aberrations are imprinted ($\simeq -10\,z_R$ from the waist position) the difference is zero. Propagation must cover a substantial fraction of the complete range of the Gouy phase, $\Delta\psi \approx \pi$, to obtain the full information about aberrations from the evaluation of intensity profiles. (c) Gouy phase change when inspecting the collimator for aberrations: in the collimated beam only a small fraction of Gouy phase change is covered, i.e. $\Delta\psi \ll \pi$, due to the large Rayleigh length of $z_R \simeq 30$ m. With a focusing lens the beam is transformed such that a propagation of $\pm 10 z_R$ around the waist position becomes possible, $\Delta\psi \approx \pi$, and the manifestation of aberrations is observed in the intensity profiles of a caustic measurement.

The electric field $E_{\text{coll.}}$ immediately after the collimator (axial coordinate $z = 0$) can be modeled with an incoming field E_0, aberration-free focusing phase $\phi_{\text{foc}}(r)$, and aberrations imprinted by the collimator summarized in the phase term $\phi_{\text{ab}}(r)$, where r denotes the radial coordinate, as

$$E_{\text{coll.}}(z = 0, r) = E_0 \exp\left(i(\phi_{\text{foc}}(r) + \phi_{\text{ab}}(r))\right) = \sum_{p=0}^{\infty} c_p \, LG_p^0(z = 0, r; q_0). \quad (2)$$

In the above equation, the aberrated field has been decomposed with complex coefficients c_p in the complete basis of Laguerre-Gaussian modes LG_p^l [29] with radial index p, azimuthal index l and common complex beam parameter $q_0 = -z_0 + iz_R$ with waist position z_0 and Rayleigh length $z_R = \pi w_0^2/\lambda$ where w_0 is the waist radius of the LG_0^0 mode (note that though q_0 and hence z_R are the same for all modes, the actual waist radius $W_0 = M w_0$ of higher-order modes is

larger, where M is the factor defined below). Here we consider for simplicity fully stigmatic (i.e., axially symmetric) beams such that $l = 0$ due to the cylindrical symmetry of the problem. The expansion in Eq. (2) can be in principle performed for any q-parameter (any choice of z_0 and z_R or w_0). However, it is advantageous for the discussion here to set the q-parameter such that z_0 and z_R have the following physical meaning: If the radius $W(z)$ of a beam with an arbitrary mode decomposition is defined through second moments of the transverse intensity distribution ('D4σ-method' according to the ISO standard [30]), any beam radius $W(z)$ follows the hyperbolic propagation law [29,31,32],

$$W(z) = W_0 \sqrt{1 + (z - z_0)^2/z_R^2}, \quad \text{with} \quad z_R = \frac{\pi w_0^2}{\lambda} = \frac{\pi W_0^2}{M^2 \lambda}, \tag{3}$$

such that z_0 and z_R (or $w_0 = W_0/M$) correspond to measurable quantities, with the factor M entering the above equation in z_R as M^2 denoted as beam quality factor.

The aberration-free focusing phase and the leading spherical aberration term can be written as

$$\phi_{\text{foc}}(r) = -\frac{k r^2}{2f}, \quad \phi_{\text{ab}}(r) \simeq S \left(\frac{r^4}{W^4} - 2 \frac{r^2}{W^2} \right), \tag{4}$$

with f being the focal distance, k the wavenumber, and W the beam radius at the position where the aberration is imprinted. The focusing effect of the r^4-term in $\phi_{\text{ab}}(r)$ is compensated by the r^2-term to isolate the contribution of the aberration alone. The parameter S characterizes the strength of spherical aberration. If in our case ($\lambda = 410$ nm, $f = 30$ mm, $W = 2.2$ mm) we would use a single thin plano-convex collimating spherical lens (flat surface facing the fiber), spherical aberrations would be as large as $S \simeq 4$ following the analytical expression of [33]. For an impinging beam with beam quality factor M_0^2 passing through optics with spherical aberrations of strength S as defined in Eq. (4), the beam quality factor is modified by an additional contribution $M_S^2 \simeq \sqrt{2}S$ as [33]

$$M^2 = \sqrt{(M_0^2)^2 + (M_S^2)^2}. \tag{5}$$

In order to understand how aberrations impact the intensity profile of the propagated beam, consider the mode-dependent phase φ_p of LG_p^0 modes, which corresponds to the accumulated phase on the beam axis relative to the plane wave,

$$\varphi_p(z) = (2p + 1)\psi(z), \quad \psi(z) = \arctan\left((z - z_0)/z_R\right), \tag{6}$$

where ψ is the Gouy phase. Because φ_p is the only mode-dependent phase term, the Gouy phase plays an essential role in the description of beam propagation [34,35]. The electric field after the collimator at a certain distance z can either be expressed by the diffraction integral or equivalently, once written in form of the mode expansion from Eq. (2), directly calculated from propagation-independent coefficients c_p with $q = z + q_0$ as

$$E_{\text{coll.}}(z, r) = \sum_{p=0}^{\infty} c_p \, \text{LG}_p^0(z, r; q). \tag{7}$$

Aberrations imprinted in the phase remain unobservable in the intensity unless propagation changes the phase relationship between different contributing modes according to Eq. (6). Since the Gouy phase ψ is the only position-dependent parameter which affects the phase change between the LG_p^0 modes, we can use ψ from Eq. (6) as a parameter to determine where aberrations present in the phase transform to intensity distortions [34]. Figure 3 (a) shows the mode-dependent phase φ_p for the first three modes and Fig. 3 (b) the phase difference relative to the fundamental Gaussian (LG_0^0) mode, which is proportional to the Gouy phase ψ. From

Eq. (6) it is clear that the dimensionless distance $(z - z_0)/z_R$ governs the propagation. The Gouy phase changes mostly within a few Rayleigh lengths around the waist position (focus) z_0. Within $\pm 10 \, z_R$, almost the full range of phase change ($\Delta \psi \simeq 0.94 \, \pi$) between different modes is covered.

In our case the collimated beam has a waist radius of $W_0 \simeq 2.2$ mm corresponding to $z_R \simeq 30$ m with a waist position $z_0 \simeq 29$ cm $\ll z_R$ lying at the HR mirror. Therefore, even if it would be possible to observe propagated beam profiles up to an arbitrary large distance after the collimator, only half of the possible phase change will be covered, $\Delta \psi \approx \pi/2$. With practically accessible propagation distances of up to few meters, i.e. $\Delta z \simeq 0.1 \, z_R$, only a small range of Gouy phase change is covered, $\Delta \psi \simeq 0.06 \, \pi$. It can be computed that spherical aberrations with $S \simeq -0.3$ appear as clear distortions in intensity, e.g. visible as a dip in the center of the intensity profile, after a propagation corresponding to a change in Gouy phase by $\Delta \psi \approx 0.85 \, \pi$ [36]. In order to observe these aberrations it is necessary to transform the beam with a dedicated lens ('M^2-lens') such that the full range of propagated beam profiles becomes accessible. This procedure corresponds to the commonly used M^2 measurement setup. By observing intensity profiles around the focus, all information about the beam mode decomposition can be extracted since the complete range of the Gouy phase propagation of $\Delta \psi \approx \pi$ is covered. The focal distance f of the M^2-lens has to be large enough for the used beam camera to resolve beam profiles around the focus created by the M^2-lens, and to avoid imprinting additional aberrations on the beam proportional to $S \propto k \, W^4 / f^3$ [33,37]. Figure 3(c) illustrates the situation in our case: for an M^2-lens of $f = 750$ mm ($S \sim 10^{-4}$ for a plano-convex lens) propagation of $\Delta z \simeq \pm 10 \, z_R$ is achieved such that $\Delta \psi \simeq 0.94 \, \pi$.

## 3.2. Influence of single-mode fiber profile

When discussing possible mode contributions from aberrations the question arises of how the fiber mode may affect imperfections in the AFR. We use a polarization-maintaining step-index single-mode fiber where the polarization-maintaining property is achieved through stress-induced birefringence [19]. The stress-inducing rods used for this purpose make the mode slightly elliptical, for our fiber resulting in the ellipticity of $\varepsilon \simeq 1.02(1)$. Since in our configuration the retroreflection preserves ellipticity, we assume for simplicity fully circular symmetric fiber modes.

For an ideal circularly symmetric weakly-guiding step-index fiber, three parameters determine the linear polarization modes: wavelength λ, core radius a and numerical aperture NA = $\sqrt{n_{clad}^2 - n_{core}^2}$ with refractive indices of the cladding, n_{clad}, and the core, n_{core} [38]. The electric field is readily calculated from the paraxial wave equation, and the V-number $V = \text{NA} \times 2 \, \pi \, a / \lambda$ determines the number of possible solutions. For $V < 2.405$ only a single solution exists such that the fiber is said to be single-mode. The electric field of this mode is piecewisely given by two Bessel functions and can be approximated by a Gaussian. However, in the expansion of this fiber mode also higher-order Laguerre-Gaussian modes contribute.

Figures 4(a) and 4(b) show the calculated and measured intensity profiles from our fiber after a propagation distance of around 30 mm (corresponding to the beam profile at the collimator with $W \simeq 2$ mm) on linear and logarithmic scales, along with a Gaussian fit to the data. On the logarithmic scale one can see that the fiber mode has larger intensity on the wings of the beam as compared to the Gaussian. Diffraction rings are expected from the calculation for radial distances $r > 2.5 \, W$ and with a relative intensity below 10^{-4}, which is not resolved by the data and outside the detector area. Nevertheless, the question arises whether these rings may be relevant for the wavefront-retracing condition in the AFR. In Fig. 4(c) the calculated mode composition for our fiber with $a = 1.5 \, \mu m$, NA = 0.10 and $\lambda = 410$ nm is shown. The q-parameter for expansion was chosen such that the contribution of LG_0^0 mode vanishes and the overlap of the LG_1^0 mode is maximized resulting in 99.58 % overlap. The contribution of higher-order modes leads to the theoretical fiber-mode beam quality of $M_0^2 \simeq 1.017$ using a self-convergent-width factor of

$F_s = 3$ as later used in the measurement, i.e. integration area within $\pm 3w$ for second-moments determination [30,39].
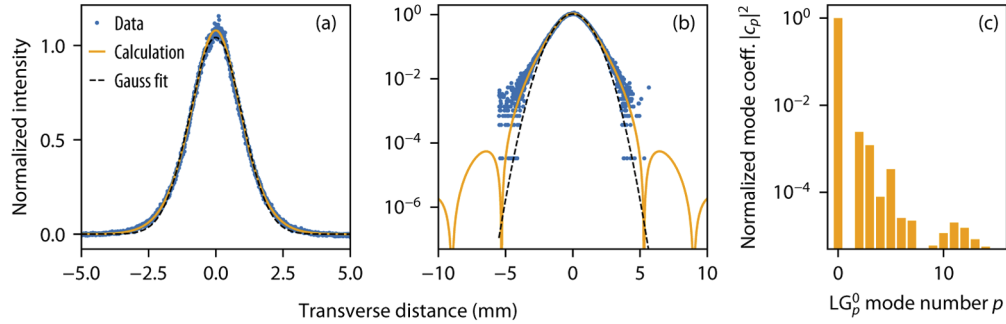

Fig. 4. Measured and calculated intensity profiles from the single-mode fiber used in the AFR [19] at a propagation distance of 30 mm ($\simeq 1000 z_R$) after the fiber tip, corresponding to the position of the collimator. Data (blue points) is depicted together with a calculation using the specified core radius and measured NA (orange line) and a Gaussian fit (black dashed line) on a linear and logarithmic scale in (a) and (b), respectively. The right plot (c) shows squared normalized mode coefficients $|c_p|^2$ of the calculated fiber mode corresponding to the overlap with LG_p^0 modes with a q-parameter that cancels $|c_1|^2$. The overlap with the Gaussian is $|c_0|^2 \simeq 0.9958$.

Since the wavefront of the beam at the fiber tip is plane, all the coefficients c_p in the mode expansion are real. Propagation to the collimator corresponds almost to the far-field ($\simeq 1000 z_R$) with a Gouy phase change of $\Delta \psi \simeq \pi/2$. The phase shift of the LG_p^0 modes relative to the LG_0^0 is then $\Delta \varphi \simeq p\pi$ which leads to a sign flip of all uneven mode coefficients. After the backpropagation the phase differences are a multiple of almost 2π with a common propagation phase for all modes. Therefore, the wavefront-retracing property of the AFR is mostly not affected by contributions of higher-order LG_p^0 modes from the fiber mode. The small residual effect from the fact that the propagation from the fiber tip to the collimator does not exactly correspond to the far-field is shown later in Fig. 6. Apart from this effect, due to the higher intensity at the wings of the beam, the fiber mode is more sensitive to possible aberrations from the collimator as compared to the Gaussian beam.

3.3. Collimator design process

For our previous collimator at 486 nm, each of the commercial achromatic doublets exhibited little spherical aberrations by itself, and the combination of two doublets found by ray tracing turned out to satisfy the requirements of the AFR without further investigation. For shorter wavelengths, we found that the three-lens collimator designed by ray tracing optics alone showed residual aberrations revealed through the caustic measurement (see Fig. 7 introduced below). Therefore, the design process was extended by wave optic propagation tools [40]. Ray tracing allows minimization of wavefront aberrations within a given aperture width, with the Gaussian beam profile not easily accounted for. For a given number of lenses a compromise has to be made between the width of the aperture employed for minimizing the wavefront deviations and the magnitude of acceptable deviations from the aberration-free wavefront. In the case of spherical aberrations, recalling Eq. (4), deviations from the aberration-free wavefront increase as $\propto r^4$ such that for larger radial distances r it becomes progressively more difficult to meet this compromise, especially at shorter wavelength. Because the wings of a laser beam extend to large r, it is a priori unclear which ray tracing criteria should be used.

Therefore, we followed an iterative design procedure together with the manufacturing company [24]. Ray tracing was used as a guidance based on the manufacturability of lenses and the requirement of effective focal length of $f \simeq 30$ mm. Using wave optics propagation [40], the designs found in this way were evaluated with simulated intensity profiles in the caustic measurement simulation. Furthermore, the electric field phase and amplitude were extracted for simulations of residual Doppler shift with optical Bloch equations. Another important design criterion explained below is the consideration of residual reflections from lens surfaces back to the fiber and to the spectroscopy region. After several iterations we found that three lenses are not enough to meet our requirements and a four-lens design was needed. In order to be able to use the same collimator for spectroscopy of all 2S-nP transitions with $n \geq 4$, the collimator was designed for wavelengths from 380 nm to 486 nm. The final collimator design with an effective focal length of $f = 31.02$ mm is shown in Fig. 5 and Table 1 lists the surface data, along with the first-order reflection analysis (see next section).
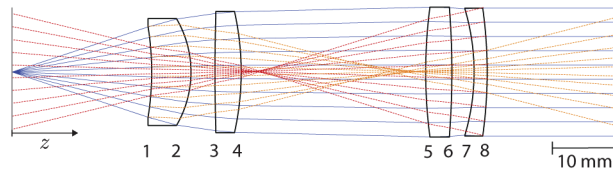
Fig. 5. Four-lens collimator design with blue solid rays illustrating the collimated beam from the fiber and numbered lens surfaces from table below. Dashed rays exemplary show reflections from the last surface (8) back into the fiber (red) and from the first surface (1) back to the HR mirror (orange). Shown lens radius corresponds to the open lens apertures.

Table 1. Lens surface data of the fused silica four-lens collimator design, along with the first-order reflection analysis. For each of the surfaces the distance z from the fiber tip, the distance d to the previous surface, and the curvature radius R are listed. The next two columns give the spatial overlap values of first-order reflection beams with the fiber mode ($z = 0$), η_{fiber}, and with the collimated beam η_{coll}. The last column lists the beam radius W_{refl} of reflections towards the HR mirror at the spectroscopy region.

Lens surface	z (mm)	d (mm)	R (mm)	η_{fiber}	η_{coll}	W_{refl} (mm)
1	21.32	–	43.89	4.0×10^{-6}	8.2×10^{-6}	21
2	27.32	6.00	16.11	0.6×10^{-6}	1.0×10^{-6}	66
3	30.99	3.67	−300.00	3.5×10^{-6}	4.1×10^{-6}	30
4	34.99	4.00	42.14	2.8×10^{-6}	3.2×10^{-6}	37
5	63.16	28.17	−75.91	2.7×10^{-6}	3.7×10^{-6}	29
6	67.16	4.00	126.05	3.2×10^{-6}	4.5×10^{-6}	30
7	70.55	3.39	33.64	0.8×10^{-6}	0.8×10^{-6}	67
8	72.55	2.00	70.10	6.4×10^{-6}	5.2×10^{-6}	28

3.3.1. Residual reflections from lens surfaces

Though all the collimator lenses are AR-coated for the desired wavelength (Layertec, reflectivity $R_{\text{AR}} < 0.15\%$ for 0–10° angle of incidence), residual reflections can lead to performance loss of the AFR. Here, we only consider single reflections from lens surfaces, since multiple reflections are strongly suppressed through the AR coating. Then, two types of reflections need to be considered. First, reflections of the forward-traveling wave on lens surfaces back towards the fiber. The part of these reflections that is coupled back into the fiber can disturb the tip-tilt

stabilization. To reduce the influence of these reflections, efficient coupling into the fiber needs to be avoided. This can be evaluated by calculating the spatial overlap integral

$$\eta_{\text{fiber}} = \frac{\left| \int E_1^* E_2 \, \mathrm{d}A \right|^2}{\int |E_1|^2 \mathrm{d}A \int |E_2|^2 \mathrm{d}A}, \tag{8}$$

where E_1 and E_2 are the electric fields of the reflected beam and the fiber mode.

The second type of reflections are reflections of the backward-traveling beam back toward the atomic spectroscopy region and the HR mirror. These reflections can influence the spectroscopy in two ways. Just like the reflection toward the fiber, an optical etalon is formed with the collimated beam, with the spatial overlap integral given by η_{coll} analogous to Eq. (8). This etalon with reflectivities $R_{\text{HR}} \sim 100\,\%$ and $\sim R_{\text{AR}} \times \eta_{\text{coll}}$ will lead to intensity variations in the spectroscopy region that depend on length and the laser frequency, which can give rise to systematic line shifts. However, since the laser intensity is stabilized to the signal of the PMT behind the HR mirror, these intensity modulations are suppressed and will instead influence the backcoupled light, possibly disturbing the tip-tilt stabilization. The reflections can also give rise to a residual Doppler effect. The more the reflections are focused near the spectroscopy region, either before or after the reflection of the HR mirror, the greater the intensity imbalance between the beams as seen by the atoms. To minimize the influence of these reflections, the design was chosen such that all reflections are diverging with a beam radius $W_{\text{refl}} \gg W_0$ at the first pass through the spectroscopy region.

The last three columns in Table 1 give the values of the spatial overlaps η_{fiber} and η_{coll} as well as the beam radius W_{refl} of the second type of reflections at the spectroscopy region for all surfaces of the collimator design. All values are smaller than $\eta < 10^{-5}$ such that with an additional suppression from the AR coating the overlaps are $< 10^{-8}$. An example of a reflection back to the fiber from the last collimator surface is illustrated with red dashed rays in Fig. 5. Orange dashed rays illustrate the reflection back to the HR mirror and the spectroscopy region (located at $z_{\text{HR}} \simeq 36$ cm and $z_{\text{atom}} \simeq 20$ cm) from the first surface, demonstrating that not only surfaces with negative curvature radii may focus the reflected beam towards the atoms. In total, three surfaces focus the second type of reflections: surfaces 1 and 3 with foci around 1 cm before the collimator end surface, and surface 5 with focus at 2 cm after the collimator but still well before the spectroscopy region. Additionally, the highly suppressed 28 combinations of reflections on two lens surfaces of the forward-traveling beam lead to 26 strongly diverging and two nearly-collimated reflected beams at the spectroscopy region.

3.3.2. Doppler shift simulations with optical Bloch equations

The collimator designs were evaluated using the wave optics propagation tool of our optics design software [40] with the fiber mode or a Gaussian beam profile as an input beam. We extracted the electric field amplitude and phase after the collimator to perform simulations of the residual Doppler shift in the AFR. For this purpose, optical Bloch equations were numerically solved for our configuration of the experiment, using the atomic system for the 2S-6P transitions in hydrogen with 10 µW of laser power. We simulated individual trajectories of atoms moving through the center of the laser beam at different angles $\alpha = 90° + \delta\alpha$, and determine the Doppler shift $\Delta\nu_D$ by fitting a Voigt function to the resulting fluorescence line shape. The atomic velocity is set to $V = 200$ m/s which, according to Eq. (1), would result in an unsuppressed collinear ($\alpha = 0°$) Doppler shift of $\Delta\nu_D = 490$ MHz and $\Delta\nu_D = 2$ MHz for $\delta\alpha = 4$ mrad. In the simulations, we evaluate the Doppler shift as a function of the fiber-collimator displacement δd_{fc} defined such that zero δd_{fc} corresponds to the collimation with maximized backcoupled light fraction. No tip-tilt misalignment of the reflected beam from the HR mirror is assumed here.

Figure 6(a) compares simulations of perfect paraxial collimation (described by the phase $\phi_{\text{foc}}(r)$ from Eq. (4)) to the four-lens collimator. Both cases are evaluated with the Gaussian beam

and the fiber mode as input beams for different angles $\delta\alpha$. The top graph shows the resulting Doppler shift $\Delta\nu_D$. The bottom graphs show two AFR beam properties: the intensity mismatch of forward- and backward-traveling beams at their beam centers, ξ_{cent}, and the backcoupled light fraction P_{bc}. In the perfectly orthogonal case (zero $\delta\alpha$, gray points and curves), the Doppler shift is strongly suppressed and found to be zero within the numerical uncertainty independent of δd_{fc}. For $\delta\alpha \neq 0$, there is one value of δd_{fc} where the Doppler shift vanishes independent of $\delta\alpha$ for each laser beam configuration. For an aberration-free Gaussian beam ("Gaussian, paraxial"), this value corresponds to the maximum backcoupled light fraction (zero δd_{fc}). As discussed in Sec. 3.2, the fiber mode mostly does not affect the wavefront-retracing property. However, since the propagation from the fiber to the collimator does not exactly correspond to the far field, the value of δd_{fc} where the Doppler shift vanishes does not exactly correspond to the point of maximal backcoupled light fraction.

Here, only single atomic trajectories are evaluated, though in the experiment a finite atomic beam divergence of 8–10 mrad (FWHM) is present. However, as Fig. 6(a) demonstrates, the Doppler shift is approximately linear in $\delta\alpha$ within the range of interest. For a symmetric atomic beam which is aligned such that, on average, the atoms cross the laser beams at an offset angle $\delta\alpha$ from the orthogonal, there is for each atom with a crossing angle of $\delta\alpha + \delta\tilde{\alpha}$ another atom with a crossing angle $\delta\alpha - \delta\tilde{\alpha}$, where $\delta\tilde{\alpha}$ is an angle within the beam divergence. This results in a partial cancellation of the overall Doppler shift, with the remaining residual Doppler shift corresponding to that of a single trajectory with angle $\delta\alpha$. As a figure of merit for the AFR performance, we evaluate the Doppler shift at the point of maximum backcoupling (zero δd_{fc}) for an angular displacement of $\delta\alpha = 4$ mrad, corresponding to the typical alignment accuracy in the experiment (see blue points and lines in Fig. 6(a)). The residual Doppler shift for the aberration-free collimation with the fiber mode is $\Delta\nu_D = 0.18$ kHz, while for the Gaussian beam the value is exactly zero. For the four-lens collimator with the Gaussian beam as the input beam, we find almost no difference to the aberration-free Gaussian beam such that $\Delta\nu_D = -0.01$ kHz. With the fiber mode, the difference to aberration-free collimation is slightly larger but small enough such that the overall effect of the fiber mode dominates the residual Doppler shift of $\Delta\nu_D = 0.23$ kHz. Comparing the Doppler shift with the intensity mismatch for different values of δd_{fc}, we find that the residual Doppler shift from the fiber mode is dominated by the induced intensity mismatch ξ_{cent} which becomes zero for the same value of δd_{fc} as the Doppler shift.

In Fig. 6(b) several simulations are shown for $\delta\alpha = 4$ mrad. For the three-lens collimator with the Gaussian beam as input (orange line) we find $\Delta\nu_D = -1.79$ kHz, and with the fiber mode as input (red line) we find $\Delta\nu_D = -2.15$ kHz. Though this residual Doppler shift still corresponds to a suppression factor $>10^5$ of the full collinear shift, its value is comparable to the uncertainty of the previous 2S-4P result [8]. Looking at the calculated backcoupled light fraction, we find $P_{bc} \simeq 88\%$ for the three-lens collimator with the fiber mode which is lower than the measured value of $94.0(1.2)\%$. We attribute this discrepancy to the not exactly known fiber parameters, as well as to the approximation that the fiber has a perfect step-index profile. The Gaussian beam with spherical aberrations of $S \simeq -0.35$ (an approximate value from Eq. (5) according to the measured beam quality factor shown later in Fig. 7) results in $\Delta\nu_D = -4.68$ kHz (green line). We find again that the residual Doppler shift is mainly caused by the intensity mismatch which vanishes approximately for the same value of δd_{fc}. Therefore, in principle, for an aberrated beam in the AFR one could adjust δd_{fc} such that the Doppler shift vanishes. However, in practice, reliable identification and adjustment of this position is challenging unless it is the point of maximized backcoupled light fraction.

Recalling the introduction, two effects may lead to a residual Doppler shift in the AFR: first, non-matching wavefronts of the forward- and backward-traveling beams, and second, imbalances of their intensities. Surprisingly, we find in our simulations, that the second effect dominates the induced Doppler shift for imperfections caused by aberrations. We do not observe significant
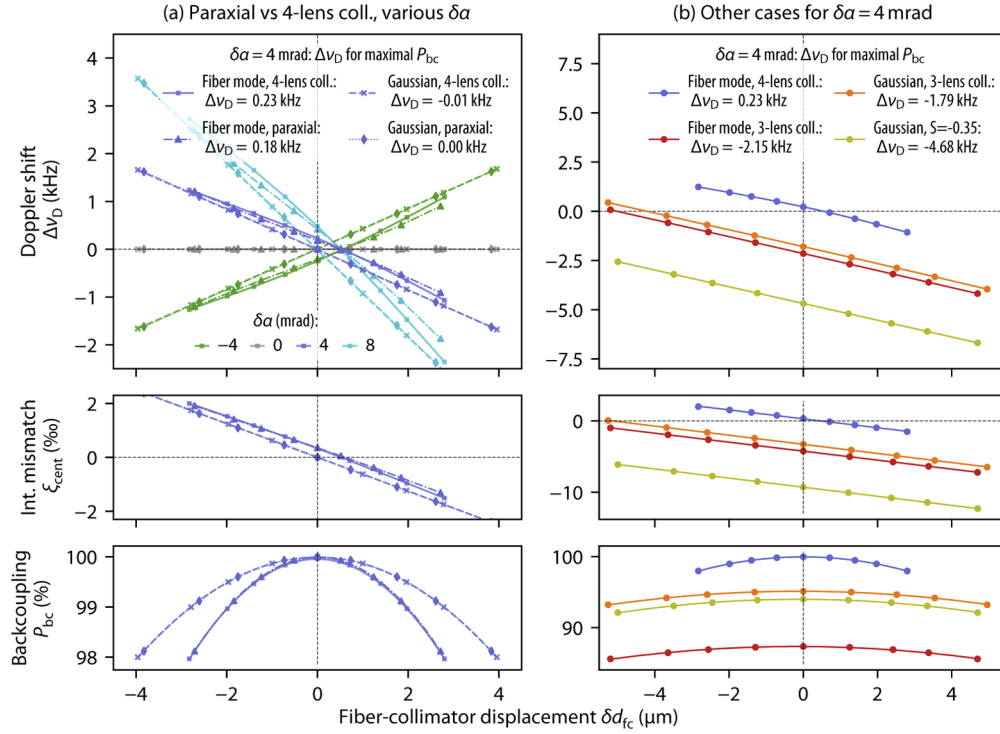
Fig. 6. The top graphs show the simulated Doppler shift $\Delta\nu_D$ for the 2S-6P transition for different AFR configurations versus the fiber-collimator displacement δd_{fc}. The bottom graphs show the intensity mismatch ξ_{cent} and the backcoupled light fraction P_{bc}, also versus δd_{fc}. (a) Aberration-free paraxial collimation compared to the four-lens collimator for different angles $\delta\alpha$. Either a Gaussian beam (dashed and dotted lines) or the fiber mode (solid and dash-dotted lines) are used as the input beam for simulations. As a figure of merit, the Doppler shift is evaluated at the maximal backcoupling (zero δd_{fc}) for $\delta\alpha = 4$ mrad (blue points and curves), demonstrating that the four-lens collimator performs almost as well as the aberration-free collimation. With the Gaussian beam as an input, no substantial difference is observed in the simulations. On the other hand, with the fiber mode as an input the residual shift of $\Delta\nu_D \simeq 0.2$ kHz is dominated by the fiber mode and not the aberrations from the collimator. (b) Simulations for $\delta\alpha = 4$ mrad. The four-lens collimator with the fiber mode (blue) is shown as a reference to (a). The three-lens collimator as well as a Gaussian beam with spherical aberrations show a residual Doppler shift of $\Delta\nu_D \simeq 2$–5 kHz, thereby limiting the performance of the AFR. This residual Doppler shift is mainly caused by the intensity mismatch at the beam center ξ_{cent} (despite the same power of forward- and backward-traveling beams), which vanishes for approximately the same value of δd_{fc} as the Doppler shift.

deviations from our simulation results if, after propagation of forward- and backward-traveling beam, the wavefront mismatch but not the intensity mismatch of both beams is fully neglected in the spectroscopy region. Therefore, though aberrations are initially imprinted in the wavefront of the beam, after propagation, they are effectively manifested in an intensity mismatch (despite equal powers of forward- and backward-traveling beams) in terms of their influence on the Doppler shift. For an aberration-free beam, the fiber-collimator distance with optimal backcoupled fraction (zero δd_{fc}) corresponds to the same distance with balanced intensities of forward- and backward-traveling beams. In the presence of aberrations, those distances are not the same, such that for zero δd_{fc} there is a residual Doppler-shift mainly due to the intensity imbalance.

3.4. Collimator-fiber system assembly and alignment

Aligning and mounting the collimator w.r.t. the fiber is important because any asymmetry present in the fiber–collimator system results in an astigmatism which distorts the wavefront-retracing condition. Correspondingly, the lenses of the collimator need to be precisely mounted without applying too much mechanical stress leading to deformation and stress-induced birefringence. The assembly of lenses was designed by the manufacturing company [24] such that the lens decenter w.r.t. the optical axis is < 30 μm, achieved with brass rings matching the lens curvatures. A retainer with a single O-ring holds the lens system in place without introducing too much deformation and birefringence (OR in Fig. 2). The fiber and collimator mounting parts are aligned w.r.t. each other using a commercial flexure translation mount (CA in in Fig. 2, Thorlabs CP1XY) allowing for centering of the fiber w.r.t. the collimator to better than 40 μm. Though we observe tip-tilt misalignment of the fiber-collimator assembly (see Sec. 4.), in simulations we find that tip-tilt misalignment does not introduce significant astigmatism as compared to decenter, so that we restrict the alignment to the dominant case of centering only.

In order to perform the collimator–fiber alignment, we measure the astigmatism through the caustic measurement setup (as shown below in Fig. 7). Combining a linear stage (Thorlabs LTS300/M) with a beam camera (UI-3380CP-M-Gl by IDS Imaging Development Systems, cover glass removed by Eureca Messtechnik), we built a caustic measurement device without additional mirrors in the setup and capable of performing a caustic measurement within one minute for the typical amount of ∼ 60 different beam positions required for our astigmatism measurement.

3.5. Measurement of collimator performance

We measured the collimator performance at 410 nm by analyzing intensity profiles in the caustic measurement shown in Fig. 7. The beam radius $W(z)$ is determined for the orthogonal x and y transverse directions according to the second-moment definition [30] with a self-convergent-width factor [39] of $F_s = 3$. This beam radius determination is performed at different positions around the focus of the M^2 lens ($f = 750\,\text{mm}$), corresponding to propagation distances from $-10\,z_R$ to $+10\,z_R$ around the waist position. From the fit according to Eq. (3) the beam waist radii $W_{0,x}$ and $W_{0,y}$, waist positions $z_{0,x}$ and $z_{0,y}$, and beam quality values M_x^2 and M_y^2 are extracted. These values determine the ellipticity ε, astigmatism a, and combined beam quality M^2 as

$$\varepsilon = \max\left(\frac{w_{0,x}}{w_{0,y}}, \frac{w_{0,y}}{w_{0,x}}\right), \quad a = \frac{z_{0,x} - z_{0,y}}{\left(z_{R,x} + z_{R,y}\right)/2}, \quad M^2 = \sqrt{M_x^2 M_y^2}. \tag{9}$$

The fits and the determined parameters are shown at the upper part of Fig. 7. The measured ellipticity of a few percent is in agreement with the slightly elliptical beam from our polarization-maintaining fiber, see Sec. 3.2. The reduced astigmatism of the four-lens collimator, $a = 0.014(4)$, was achieved with the help of alignment described in Sec. 3.4 compared to the three-lens collimator with $a = 0.216(5)$ where the collimator was aligned with the help of centering the observed distortions in the intensity profiles. For the three-lens collimator we find $M^2 = 1.124(6)$ which
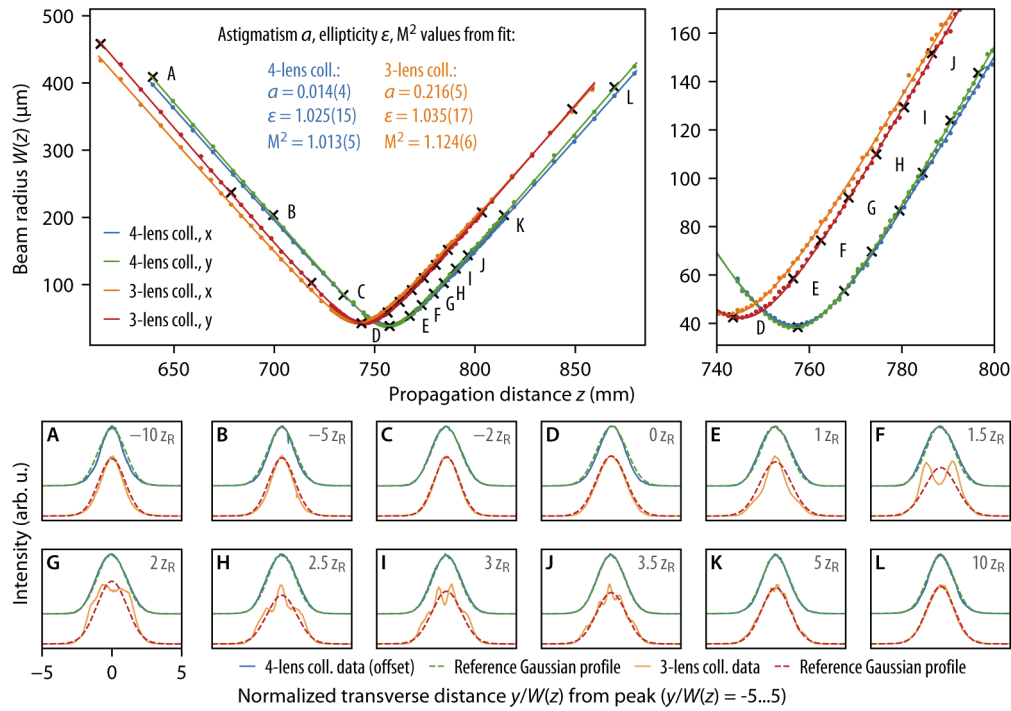
Fig. 7. Caustic measurement of the three-lens and four-lens collimators at 410 nm. At the top, the beam radius $W(z)$, obtained from second-order moments in the x and y directions, is plotted against the propagation distance z (with different offset for the two collimators) after the $f = 750$ mm focusing lens, with a zoomed region of up to four Rayleigh lengths after the focus where distortions due to spherical aberrations are expected. The fitted beam quality value for the three-lens collimator is $M^2 = 1.124(6)$ due to spherical aberrations with $|S| \simeq 0.34$, whereas for the four-lens collimator the beam quality of $M^2 = 1.013(5)$ is not limited by spherical aberrations but by the fiber mode profile described in Sec. 3.2. At the bottom, normalized intensity profiles at selected propagation distances A to L (from $-10\,z_R$ to $+10\,z_R$, marked on the top plot) are depicted, along with reference Gaussian beams of $1/e^2$ intensity radius $W(z)$.

corresponds to $|S| = 0.33(1)$ according to Eq. (5). Aberrations are also revealed as distortions in intensity around the focus after the M^2 lens, see bottom of Fig. 7 where the intensity profiles at selected positions A to L marked on the top are shown. For the three-lens collimator we observe the characteristic intensity profiles for a beam with spherical aberrations [36]. Note that distortions in intensity appear only in the region between z_R and $4\,z_R$ after the focus, which demonstrates that the manifestation of aberrations cannot be readily observed in intensity of collimated beam without the caustic measurement. In the simulations of caustic intensity profiles for the given three-lens collimator design, we find a larger dip depth and more distorted intensity profiles than observed, which we attribute to high sensitivity to single-mode fiber input parameters. For the four-lens collimator, no beam profile distortions are observed in agreement with simulations using the given lens design, and the beam quality factor $M^2 = 1.013(5)$ is limited by the fiber profile as calculated in Sec. 3.2.

The collimated beam intensity profiles in the spectroscopy region (corresponding to 12 cm propagation distance after the collimator) are shown in Figs. 8 (a) and 8 (b) for the three-lens and four-lens collimator, respectively. Though no performance shortcomings of the four-lens collimator are observed in the caustic measurement, a weak residual 'orange-peel' structure

is observed on the collimated beam of both collimators, which is more pronounced for the four-lens collimator. This structure is barely observed on cuts through intensity profiles as shown in Fig. 8(c). We observed similar but much stronger deviations in beam profiles from aspheric lenses where these mid-spatial frequency errors are more pronounced, as well as for some other collimators. It is important to note that these lens imperfections imprint phase distortions which may disturb the wavefront-retracing property of the AFR. After propagation, these phase distortions transform into intensity distortions and may introduce a residual Doppler shift. Therefore, it is important to ensure best possible lens polishing quality, minimizing mid-spatial frequency errors. In our case, the lens surfaces and polishing processes responsible for deviations observed in Fig. 8 (b) could not yet be identified and remain under investigation together with the manufacturer [24]. We believe that the observed orange-peel structure originates from residual grinding structures on some lens surface which are not fully removed by polishing. Ultimately, for our experiment only the velocity-resolved spectroscopy measurement provides certainty on the suppression factor of the Doppler shift. A recent precision measurement of the 2S-6P transition, using the four-lens collimator discussed here, is currently analyzed and will be subject of a later publication. In the preliminary data analysis we see no evidence for a residual Doppler shift within the uncertainty of the measurement ($\lesssim 1$ kHz).
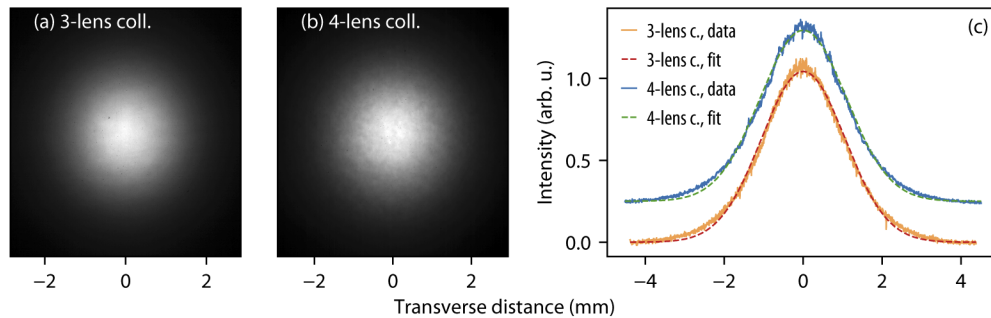
Fig. 8. Measured beam profile of the collimated beam in the spectroscopy region of the AFR (12 cm after the collimator) for: (a) 3-lens collimator, (b) 4-lens collimator. A weak 'orange-peel' structure is visible in both beam profiles, but more pronounced on the 4-lens collimator beam profile. Cuts through the beam profiles are shown in (c) along with a Gaussian fit to the data (offset for 4-lens collimator). Note that aberrations present in the phase at this position are not observed in the shown intensity profile, but are revealed through the caustic measurement as demonstrated in Fig. 7.

As discussed at the beginning of this section, the backcoupled light fraction gives an important figure of merit of the collimator performance. Compared to the three-lens collimator with a backcoupled fraction of 94.0(1.2) %, the backcoupled light fraction of the four-lens collimator is measured to be 99.3(1.2) %. Note that this number gives the spatial overlap of the forward- and backward-traveling beams in the AFR, with the known transmission losses of the beam path from the spectroscopy region to the backcoupling APD taken into account. The uncertainty of 1.2 % is deduced from the quadrature sum of uncertainties for position-dependent photodiode sensitivity, beamsplitter transmission, fiber attenuation, as well as AR coating uncertainties of the fiber coupling lens, fiber tips, and collimator lenses.

4.   Retroreflection control and stabilization

In order to achieve the wavefront-retracing retroreflection in the AFR, it is necessary to adjust the distance between the fiber and the collimator (collimation distance) such that the position of the flat wavefront of the collimated beam is at the HR mirror. Moreover, the horizontal and vertical

(tip-tilt) directions of the HR mirror need to be oriented such that the wave vectors of the forward and backward propagating waves are antiparallel to each other. If both conditions (collimation and tip-tilt alignment) are optimized, the backcoupled light fraction is maximized.

The stabilization of the HR mirror tip-tilt orientation is described in detail in the previous work [11]. In short, modulating the two piezo actuators for the tip-tilt movement of the HR mirror mount [18] with weak signals of different frequencies (producing maximal angular misalignment of $\sim \pm 1$ μrad) and detecting this modulation in the backcoupled light with two lock-in amplifiers, two error signals are generated which are used for the tip and tilt stabilization feedback loops. We tried improving the bandwidth of the feedback by using higher modulation frequencies. Mechanical resonances cause a crosstalk between the otherwise linearly independent horizontal and vertical piezo actuators. In order to find frequencies with minimal crosstalk between horizontal and vertical modulation, we measure the corresponding transfer functions of the HR mirror assembly. For this measurement we use an auxiliary laser beam hitting the HR mirror from the back side to allow for an in-situ measurement (with PMT being removed) under a small ($\simeq 5°$) angle, and detect the reflection with a position-sensitive detector while sweeping the frequency of horizontal and vertical piezo actuators. Though higher modulation frequencies of 1.52 kHz (vertical) and 2.09 kHz (horizontal) with minimal crosstalk (typically 10–30 % amplitude ratio of horizontal to vertical error signals) could be identified, the feedback bandwidth could not be improved due to large mechanical resonances around 30 Hz caused by the rotatable geometry of the whole AFR setup.

Figure 9 shows the performance of the tip-tilt stabilization, where in (a) and (b) the in-loop error signals are plotted. The bandwidth of stabilization as deduced from the in-loop error signals is around 10 Hz. However, no significant noise suppression is observed in the spectrum of the backcoupled light shown in (c), with even a slight increase of noise visible for low frequencies when the tip-tilt stabilization is switched on. Only a small decrease of noise is visible on the backcoupled light for resonances around 30 Hz. Apart from Rayleigh scattering from fiber discussed below, the unobserved noise suppression in the backcoupled light could originate from the large amount of noise common to both directions which cannot be suppressed due to large cross-talk. Though for inspection of this issue no out-of-loop measurement of the tip-tilt
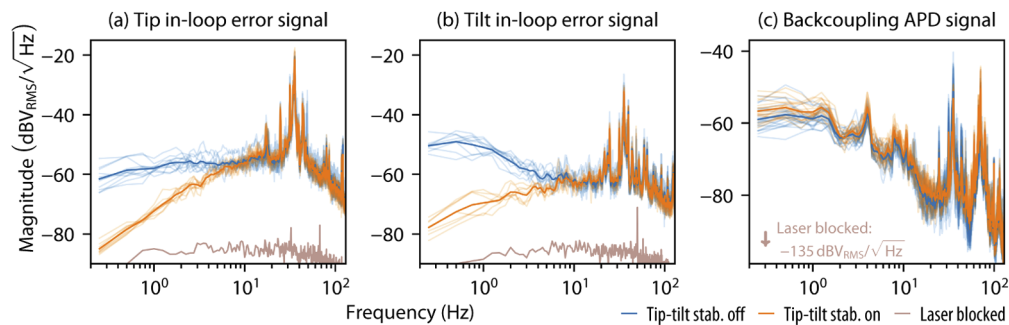
Fig. 9. Performance of the tip-tilt stabilization of the AFR (with 2nd intensity stabilization switched on). Spectra of the in-loop error signals produced by the lock-in amplifiers (1 ms time constant) for the horizontal and vertical (tip and tilt) feedbacks of the HR mirror are shown in (a) and (b). The spectrum of the backcoupled light on the 'Backcoupling APD' (see Fig. 1) is shown in (c). All spectra are shown with tip-tilt stabilization switched on (orange line), off (blue line) and with the laser blocked (gray line). Each faint line is a 15 s average with a resolution bandwidth of 0.25 Hz, whereas heavy lines are the average of all data. Large resonances around 30 Hz are observed on all signals, limiting the feedback bandwidth to around 10 Hz as deduced from the in-loop error signals.

stabilization is available in our setup, the performance of the tip-tilt feedback is clearly observed in the backcoupled light when scanning the piezo actuator controlling the fiber-collimator distance as described below and shown in Fig. 10. Likewise, during a typical hour-long precision spectroscopy measurement, the tip-tilt feedback maintains the retro-reflecting condition.
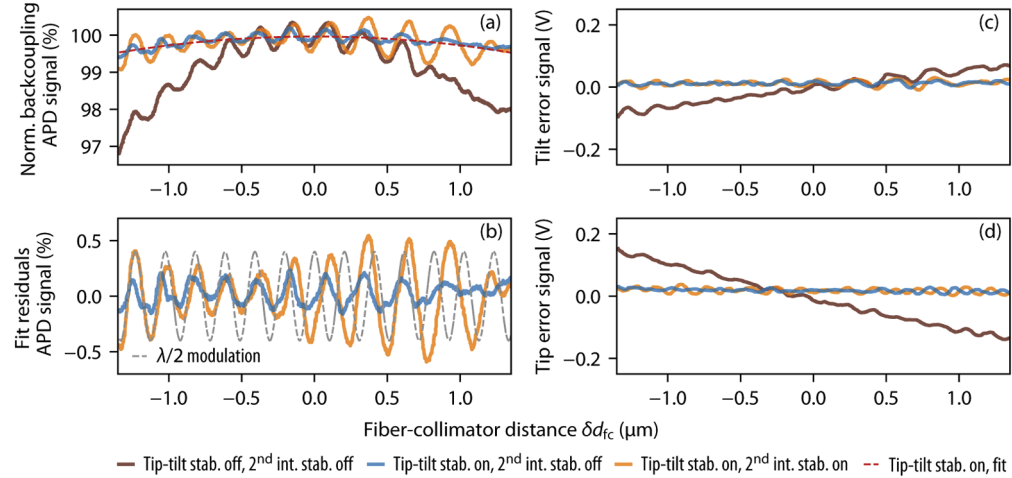
Fig. 10. Demonstration of the improved fiber-collimator distance control using a piezo actuator. All plots show the recorded data when scanning the voltage of the piezo actuator with a frequency of 1 Hz over an averaging time of 30 s. The common *x*-axis has been converted from the applied voltage and leverage factor to the fiber-collimator displacement δd_{fc}, with zero δd_{fc} corresponding to maximum backcoupling. In (a) the normalized signal of the backcoupled light is shown. If the tip-tilt stabilization is switched off (brown curves), clear tip-tilt misalignment is observed on the in-loop error signals of the tip-tilt stabilization shown in (c) and (d), leading to a large drop in the backcoupled light fraction of $\sim 3\%$ in (a) over the full distance range. With tip-tilt being stabilized (blue and orange curves), this drop is reduced to $\sim 0.5\%$ in agreement with simulations from Fig. 6. The dashed curve in (a) shows a quadratic fit to the data with tip-tilt stabilization switched on. Clear modulation is observed on all of the signals, originating from Rayleigh scattering inside the fiber leading to an etalon-like effect. Along with the fit residuals of the backcoupled fraction in (b), the expected $\lambda/2$ modulation is drawn (dashed gray curve) which also reveals the nonlinearity of the piezo actuator. As expected, the modulation is stronger when the 2nd intensity stabilization (to the PMT after the HR mirror) is switched on (orange curve), as compared to the case with intensity not stabilized (blue curve).

In the previous setup [11] the collimation distance was adjusted by using a remote-controlled motor and maximizing the observed signal on the backcoupling APD. With this procedure the backcoupled signal could typically be optimized within $\sim 1\%$. We improved the distance control by adding a piezo actuator to the precision motor, which is now used for pre-alignment only. In order to determine the optimal piezo voltage, we typically scan the applied voltage with a frequency of 1 Hz over a period of 30 s such that the fluctuations on the backcoupling APD are averaged out, see Fig. 10. Due to the not exactly on axis translation of the fiber, we observe tip-tilt misalignment on the in-loop error signals shown in (c) and (d), resulting in a large drop of the backcoupled light fraction ($\sim 3\%$) shown in (a) with tip-tilt stabilization switched off (brown curves). With the tip-tilt stabilization switched on (blue and orange curves), the drop of the backcoupled light fraction by $\pm 0.5\%$ for ± 1.5 µm around $\delta d_{\text{fc}} = 0$ agrees with simulations from Fig. 6. From the fitted dashed line the optimal piezo voltage is determined, allowing to set the fiber-collimator distance to within $\sim \pm 0.2$ µm of the optimal value corresponding to $\pm 0.1\%$ of

the maximum backcoupled light fraction value. In our setup we observe only slow drifts of the optimal collimation distance on the order of 0.2 μm per hour (correlated with temperature) such that typically an adjustment is performed every 1–2 hours with no need of active stabilization.

The observed modulation on the backcoupled light fraction in Fig. 10(a) demonstrates how in addition to the precise distance control, the piezo actuator provides the possibility to inspect the AFR for optical etalons. The corresponding $\lambda/2$ modulation is depicted along with fit residuals in (b), not exactly matching all the data due to expected nonlinearities of the piezo actuator of $\sim 20\,\%$ over the full range. In order to avoid etalons, we use only AR-coated optics and place all photo-detectors at large angles ($\gtrsim 10°$). The fiber tips are angle-cleaved under 8° and AR-coated. After a thorough investigation, we found that the modulation we observe originates from Rayleigh scattering inside the fiber. A small fraction on the order of 10^{-3} of the scattered light from randomly distributed scattering points inside the fused silica of the fiber is guided forward and backward in the fiber mode [41–43], interfering with the strong reflection from the HR mirror. As expected, stabilizing the intensity after the fiber leads to an increased modulation (orange curves) as compared to the case with the stabilization switched off (blue curves). The phasor of total back scattered Rayleigh light corresponds to a random walk due to the random distribution of scattering points. Therefore, the modulation depth of the backcoupled light increases with the square-root of the fiber length, and we use an as short as possible fiber. The detailed report of our investigation of the etalon-like effect from Rayleigh scattering in fiber will be subject of another publication.

5. Intensity stabilization

Since the spectroscopy signal depends on the intensity of the exciting laser beams, it is advantageous to implement an intensity stabilization in the AFR. Various sources like pointing fluctuations, polarization drifts, electronic noise in the laser system or frequency-dependent AOM efficiencies lead to intensity fluctuations already before the light reaches the AFR fiber. In the previous setup only the intensity of this light before the fiber was stabilized [11]. However, the intensity of the wavefront-retracing beams in the AFR is then still affected by the coupling efficiency of the AFR fiber, subject to pointing fluctuations, as well as by the frequency-dependent interference from the Rayleigh scattering mentioned above. In order to stabilize the intensity of the wavefront-retracing beams, we use the summed signal of all four quadrants of the PMT behind the HR mirror (see Fig. 1). Due to the low power reaching the PMT (70–400 pW) and the resulting large shot noise, only a low-bandwidth stabilization can be achieved such that the high-bandwidth first intensity stabilization (with PD1 in Fig. 1 serving as detector) is still needed to suppress other noise. Two electro-optic modulators (EOM 1 and EOM 2 in Fig. 1, Conoptics KD*P Crystal Series 350-50) are used as voltage-controlled wave plates and, combined with polarizing beamsplitters, serve as actuators for the two intensity stabilizations. A low-pass filter is placed before EOM 2 to adapt for lower feedback bandwidth.

Figure 11 shows the performance of the two intensity stabilizations by comparing the spectra for the corresponding stabilization switched on (orange line) and off (blue line). In (a) the spectrum of the out-of-loop detector PD3 demonstrates the $\sim 30\,$kHz bandwidth of the first intensity stabilization (with the second intensity stabilization switched off). The spectrum of the PMT signal which is the in-loop detector of the second intensity stabilization is shown in (b), where the feedback bandwidth of $\sim 10\,$Hz is observed from the merging point of the blue and orange data lines. The second intensity stabilization imprints the noise of the stabilized signal on the PMT to the light before fiber observed on the spectrum of PD3 signal in (c). Note that also shot noise from the PMT signal is imprinted which cannot be fully avoided. Using a low-pass filter with a corner frequency of 80 Hz in the second intensity stabilization we found a compromise between a sufficient suppression of noise and an acceptable additional imprinting of shot noise at lower frequencies.
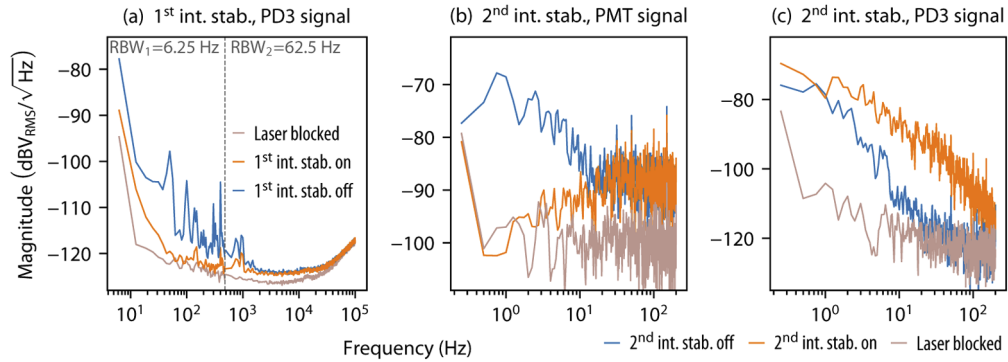
Fig. 11. Spectra of the PMT and PD3 photodetector signals showing the performance of the two intensity stabilizations of the AFR, shown for active stabilization on (orange line) or off (blue line) along with the background noise (gray line). (a): Spectrum on the out-of-loop PD3 detector demonstrating the performance of the first high-bandwidth (~30 kHz) intensity stabilization to PD1 (with second intensity stabilization switched off). The frequency interval up to 500 Hz is plotted with a resolution bandwidth (RBW_1) of 6.25 Hz and with $RBW_2 = 62.5$ Hz for higher frequencies. (b) and (c): Second intensity stabilization of wavefront-retracing beams using the PMT signal after the HR mirror (with first intensity stabilization switched on). The in-loop PMT spectrum in (b) demonstrates the bandwidth of around 10 Hz while additional noise is imprinted on PD3 as shown in (c).

When scanning the atomic resonance, at each point the frequency applied to the AOM in Fig. 1 is switched, thereby causing a short dead time (in our case ∼ 400 μs using the signal generator Rohde & Schwarz SMC100A) where no light is diffracted by the AOM. The error signal generated from noise during that dead time perturbs the feedback loops. To avoid this, we use a pulse generator triggered to frequency switching to place the feedback loops on hold during and after the dead time, adapted to each of the feedback loops (20 ms for 1st int. stab., 22 ms for 2nd int. stab., 50 ms for tip-tilt stab.).

Furthermore, we implemented the possibility to automatically switch the power of the spectroscopy laser beams by using digital step attenuators (Mini-Circuits ZX76-31R5A-PPS+) connected in series at the output of the photodiodes. In this way, the signal levels of the feedback loops remain unchanged without the need to modify the feedback loop parameters. The power switching allows us to perform simultaneous spectroscopy measurements with different laser powers, thereby investigating the effect of light-force induced line distortions and systematic frequency shifts in the spectroscopy measurement [9].

6. Polarization monitor

In our experiment, we try to achieve the best possible linear polarization of the wavefront-retracing beams. The residual circularly polarized light leads to the first-order Zeeman shift which vanishes for fully linearly polarized light. The linear polarization rotation angle ψ matters for other effects like quantum interference [8]. One way to achieve a well-controlled polarization in the AFR would be to place a polarizer after the collimator. However, such a polarizer might lead to optical etalons, wavefront distortions, and residual intensity fluctuations, and requires additional space currently not available in our setup. Therefore, we choose to work only with a well-characterized polarization-maintaining (PM) fiber.

In the following, we use the Stokes formalism for the description of the residual circularly polarized light given by S_3/S_0, where S_0 is the total intensity and S_3 the intensity difference between right and left circularly polarized light [44]. The linear polarization rotation angle ψ

is given by the other two Stokes parameters as $\tan 2\psi = S_2/S_1$. For fully polarized light (zero unpolarized light fraction), the polarization extinction ratio PER of the beam is related to the residual circular polarized light fraction as $|S_3/S_0| \sim 2\sqrt{1/\text{PER}}$ for PER $\gg 1$.

In order to achieve a high PER after a PM fiber, it is important to use incoming light with a high PER, and to align the linear polarization rotation angle of the incoming light to the polarization-maintaining axis of the fiber. For our PM fiber, this alignment has to be better than 1°, which we achieve by placing the polarizers in the PSPU (see Fig. 1) on rotation mounts. Furthermore, we find that the coupling lens as well as mirrors and beamsplitters after the polarizers may distort the input polarization due to stress-induced birefringence. We minimize this effect by also placing the fiber onto a rotation mount, and systematically varying the orientation of both the polarizers and the fiber mount. For their optimal orientations, the polarization is aligned to both the stress-induced birefringence axis of optical components after the polarizers (such that the resulting effect from their birefringence is minimized), and the polarization-maintaining axis of the fiber.

Typically, for PM fibers in the near UV, the specified PER of the output polarization (for optimal alignment of input polarization) is around 20 dB, corresponding to a circularly polarized fraction of $|S_3/S_0| < 20\,\%$. For our PM fibers, we find that stress-induced birefringence at the fiber connectors mostly limits the achieved extinction ratio and that in a sample of commercial, connectorized fibers some have a higher extinction ratio of up to 28 dB corresponding to $|S_3/S_0| < 8\,\%$. Furthermore, we observe that by thermally isolating the part of the fiber outside of vacuum, only slow polarization drifts occur on the timescale of hours.

To monitor the polarization in the AFR, we implemented polarimetry of the backcoupled light by placing a polarimeter (Schäfter+Kirchhoff SK010PA-UV) in the unused beam path before BS 2 as depicted in Fig. 1. Note that the same information could be obtained from polarimetry of the light after the HR mirror. However, this would further increase the complexity of the setup and require an in-vacuum polarimeter for < 100 pW of laser power. In the following, we summarize how the measured polarization of backcoupled light relates to the polarization after the collimator in the AFR. Before the light reaches the polarimeter, it passes various optical components, the fiber, and the collimator in the forward- and backward-traveling directions. The total birefringence effect of all components on the same path for the forward- and backward-traveling directions can be described by a single retardance δ with the birefringence axis oriented at an angle β to the vertical. Consider first a perfect incoming horizontal or vertical linear polarization, $(S_1/S_0)_\text{in} = \pm 1$ and $(S_2/S_0)_\text{in} = (S_3/S_0)_\text{in} = 0$. The forward propagation results in a circularly polarized fraction after the collimator as seen by the atoms of $(S_3/S_0)_\text{atom} = \pm \sin(2\beta)\sin\delta$. The backcoupled light has then a circularly polarized fraction of $(S_3/S_0)_\text{back} = \mp \sin(2\beta)\sin(2\delta) \simeq \mp 2(S_3/S_0)_\text{atom}$ (note the sign change due to the opposite propagation direction), where in the last step we consider our case of small δ such that the polarization remains approximately linear. Accounting for a small circularly polarized fraction, $|(S_3/S_0)_\text{in}| \ll 1$, before the first common component (e.g. in our setup between BS 2 and BS 3 in Fig. 1, where we measure $|(S_3/S_0)_\text{in}| \lesssim 3\,\%$) gives

$$(S_3/S_0)_\text{back} \simeq -2(S_3/S_0)_\text{atom} + (S_3/S_0)_\text{in}. \tag{10}$$

The linear polarization rotation angle in the AFR is coarsely given by the orientation of the polarization-maintaining axis of the fiber, which we align by using the rotation mount of the fiber-collimator system (RM in Fig. 2). From the polarimetry of the backcoupled light we can then deduce the variation of the linear polarization angle. Similar to the above consideration, one finds that the change in the linear polarization angle of the backcoupled light, $\Delta\psi_\text{back}$, relates to the change $\Delta\psi_\text{atom}$ as seen by atoms as

$$\Delta\psi_\text{back} \simeq -4\,\Delta\psi_\text{atom}. \tag{11}$$

Typically, mirrors and non-polarizing beamsplitters before the polarimeter are subject to stress-induced birefringence, as well as a polarization-dependent transmission and reflectivity.

We here find that the latter are unbalanced on the level of 2 % and thus negligible. Note that Eqs. (10)–(11) do not include the stress-induced birefringence of uncommon components for the forward- and backward-traveling directions, e.g. BS 2 may introduce a different retardance in transmission than in reflection. Therefore, the remaining distinct path of the backward-traveling beam to the polarimeter needs to be taken into account separately. We can again model the total birefringence of optical components between the place where $(S_3/S_0)_{in}$ is measured and the polarimeter with a single wave plate of retardance δ_{BS} and orientation β_{BS}. For mostly horizontal or vertical linear polarization ($|S_1/S_0| \simeq 1$, $|S_2/S_0| \ll 1$, $|S_3/S_0| \ll 1$) as well as small δ_{BS} (in our setup $\delta_{BS} \lesssim 0.3$ rad) and small β_{BS} (the optics mounts of our setup predominantly lead to horizontal or vertical forces, and we find $\beta_{BS} \lesssim 0.1$ rad), the measured Stokes parameters are related to the Stokes parameters of the backcoupled light from Eqs. (10)–(11) as

$$
\begin{aligned}
(S_1/S_0)_{back} &\simeq (S_1/S_0)_{meas} + 2\delta_{BS}\beta_{BS}(S_3/S_0)_{meas}, \\
(S_2/S_0)_{back} &\simeq (S_2/S_0)_{meas} - \delta_{BS}(S_3/S_0)_{meas}, \\
(S_3/S_0)_{back} &\simeq (S_3/S_0)_{meas} + \delta_{BS}(S_2/S_0)_{meas} - 2\delta_{BS}\beta_{BS}(S_1/S_0)_{meas}.
\end{aligned} \tag{12}
$$

Eqs. (10)–(12) allow to monitor the polarization as seen by atoms from polarimetry of backcoupled light and the characterized stress-induced birefringence of optical components before the polarimeter. We confirmed this method by measuring the polarization directly after the collimator (which blocks the laser beam before the HR mirror and therefore cannot be done in-situ), and comparing it to the derived result from the subsequent measurement of the backcoupled polarization. Based on the uncertainties for Stokes parameter measurements (~ 1 %) combined with uncertainties for δ_{BS} and β_{BS} (~ 30 mrad), we estimate the absolute accuracy on deducing $(S_3/S_0)_{atom}$ to ~ 2 %, and to $\sim 0.1°$ or ~ 2 mrad for $\Delta\psi_{back}$.
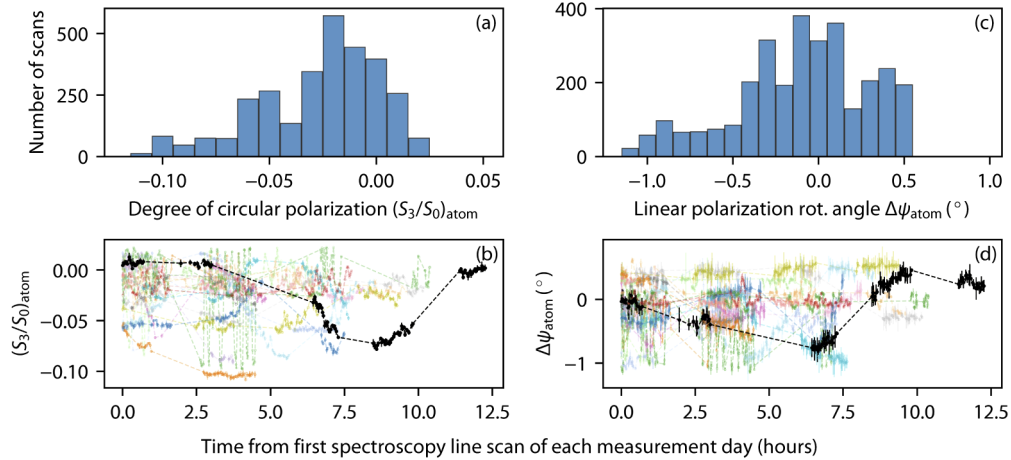
Fig. 12. Polarization in the AFR (as seen by the atoms) as deduced from polarimetry of backcoupled light according to Eqs. (10)–(12). On the left, the circular polarization fraction $(S_3/S_0)_{atom}$ is shown, on the right the variation of the linear polarization rotation angle $\Delta\psi_{atom}$. The top histograms summarize polarization data from 3035 spectroscopy line scans (22 measurement days). The circular polarization fraction is typically $|(S_3/S_0)_{atom}| \lesssim 8$ % corresponding to PER $\gtrsim 28$ dB, whereas the linear polarization rotation angle varies by $\sim 1°$. At the bottom, polarimetry data for each spectroscopy line scan are plotted versus time in faint colors for several days (from the first spectroscopy line scan of the day), with one exemplary day (227 line scans) being highlighted in black. Error bars show the variation within a minute-long line scan. The absolute accuracy of $(S_3/S_0)_{atom}$ and $\Delta\psi_{atom}$ is ~ 2 % and $\sim 0.1°$, respectively.

We continuously took polarimetry data during our hydrogen spectroscopy measurement campaign. In Fig. 12, the polarization after the collimator (as seen by the atoms) is shown, as deduced from polarimetry of the backcoupled light according to the above equations. The top histograms show the values for $(S_3/S_0)_{atom}$ and $\Delta\psi_{atom}$ for 22 measurement days with a total number of 3035 spectroscopy line scans. For most of the data we observe $|(S_3/S_0)_{atom}| \lesssim 8\,\%$ corresponding to PER $\gtrsim 28$ dB. Note that $(S_3/S_0)_{atom}$ does not center around zero because of an offset introduced by the stress-induced birefringence of the fiber connectors and the collimator. The linear polarization rotation angle varies by $\lesssim 1°$. The time variation of polarization data is shown on the bottom of Fig. 12, where in (b) the circularly polarized fraction and in (d) the linear polarization rotation angle are plotted for each measurement day starting from the first spectroscopy line scan, with one single day highlighted in black. Due to slow drifts on the timescale of hours and well-known polarization deduced from in-situ monitoring, it is possible, if needed, to extract spectroscopy data with $(S_3/S_0)_{atom} \lesssim 2\,\%$ corresponding to PER $\gtrsim 40$ dB.

7.   Conclusions and outlook

In this work, we have shown that in order to extend the previous AFR at 486 nm to shorter wavelength in the near UV, particular attention should be given to minimizing aberrations produced by the collimator. We described how in the framework of a caustic measurement, weak aberrations are revealed by analyzing intensity profiles around the focus of an additional lens. Our three-lens collimator demonstrates how aberrations limiting the performance of the AFR are not observed in the intensity of a collimated beam, but are clearly visible with the caustic measurement method. We extended the design process of the collimator by simulating the effect of residual aberrations on Doppler-shift suppression using wave optics propagation, thereby including the influence of the wings of the fiber mode contributing to aberrations. The four-lens collimator design shows no significant differences in simulations compared to the perfect Gaussian beam, and no aberrations are observed in the caustic measurement. The measured backcoupled light fraction using this collimator in the AFR is consistent with 100 %. The simulated Doppler shift of $\Delta\nu_D \simeq 0.2$ kHz for spectroscopy of the 2S-6P transition in hydrogen with our apparatus, as well as the measured beam quality factor of $M^2 \simeq 1.02$, are limited by higher-order modes from the single-mode fiber.

Together with the extension of the AFR to shorter wavelengths, this work also reports other improvements in the AFR. The fiber–collimator distance, of crucial importance to achieve a wavefront-retracing retroreflection, is precisely controlled with a piezo actuator. The intensity of the wavefront-retracing beams is stabilized with a photomultiplier after the highly reflective mirror. Furthermore, the purity of linear polarization is deduced from polarimetry of the backcoupled light allowing the monitoring of slow drifts in the residual fraction of circularly polarized light as well as the linear polarization rotation angle. This makes it possible to use the AFR with linear polarization of known extinction ratio of up to 40 dB.

With the improved active fiber-based retroreflector presented in this work we took precision spectroscopy data of the 2S-6P transition in hydrogen and are currently in the process of data analysis. This precision measurement will be subject of a future publication, with the achieved suppression of the first-order Doppler shift serving as a performance marker for the collimator. The AFR presented in this publication can be used for all 2S-nP transition measurements in the wavelength range 380 nm to 486 nm corresponding to $4 \leq n \leq 10$. In the future, we also plan to measure the analogous transitions in atomic deuterium [45,46]. Since for this measurement also other polarization states are helpful, we are exploring different possibilities on integrating circular polarization in our AFR setup.

Disclosures. The authors declare no conflicts of interest.

References

1. R. Carriles, D. N. Schafer, K. E. Sheetz, J. J. Field, R. Cisek, V. Barzda, A. W. Sylvester, and J. A. Squier, "Invited Review Article: Imaging techniques for harmonic and multiphoton absorption fluorescence microscopy," Rev. Sci. Instrum. **80**(8), 081101 (2009).

2. J. F. Sherson, C. Weitenberg, M. Endres, M. Cheneau, I. Bloch, and S. Kuhr, "Single-atom-resolved fluorescence imaging of an atomic Mott insulator," Nature **467**(7311), 68–72 (2010).

3. E. A. Salim, S. C. Caliga, J. B. Pfeiffer, and D. Z. Anderson, "High-Resolution Imaging and Optical Control of Bose-Einstein Condensates in an Atom Chip Magnetic Trap," Appl. Phys. Lett. **102**(8), 084104 (2013).

4. T. van Leent, M. Bock, R. Garthoff, K. Redeker, W. Zhang, T. Bauer, W. Rosenfeld, C. Becher, and H. Weinfurter, "Long-Distance Distribution of Atom-Photon Entanglement at Telecom Wavelength," Phys. Rev. Lett. **124**(1), 010510 (2020).

5. R. H. Parker, C. Yu, W. Zhong, B. Estey, and H. Müller, "Measurement of the fine-structure constant as a test of the Standard Model," Science **360**(6385), 191–195 (2018).

6. V. Schkolnik, B. Leykauf, M. Hauth, C. Freier, and A. Peters, "The effect of wavefront aberrations in atom interferometry," Appl. Phys. B **120**(2), 311–316 (2015).

7. A. Gauguet, B. Canuel, T. Lévèque, W. Chaibi, and A. Landragin, "Characterization and limits of a cold-atom Sagnac interferometer," Phys. Rev. A **80**(6), 063604 (2009).

8. A. Beyer, L. Maisenbacher, A. Matveev, R. Pohl, K. Khabarova, A. Grinin, T. Lamour, D. C. Yost, T. W. Hänsch, N. Kolachevsky, and T. Udem, "The Rydberg constant and proton size from atomic hydrogen," Science **358**(6359), 79–85 (2017).

9. X. Zheng, Y. R. Sun, J.-J. Chen, J.-L. Wen, and S.-M. Hu, "Light-force-induced shift in laser spectroscopy of atomic helium," Phys. Rev. A **99**(3), 032506 (2019).

10. L. Semeria, P. Jansen, G.-M. Camenisch, F. Mellini, H. Schmutz, and F. Merkt, "Precision Measurements in Few-Electron Molecules: The Ionization Energy of Metastable ^{4}He$_2$ and the First Rotational Interval of ^{4}He$_2^+$," Phys. Rev. Lett. **124**(21), 213001 (2020).

11. A. Beyer, L. Maisenbacher, A. Matveev, R. Pohl, K. Khabarova, Y. Chang, A. Grinin, T. Lamour, T. Shi, D. C. Yost, T. Udem, T. W. Hänsch, and N. Kolachevsky, "Active fiber-based retroreflector providing phase-retracing anti-parallel laser beams for precision spectroscopy," Opt. Express **24**(15), 17470 (2016).

12. W. T. Welford, *Aberrations of Optical Systems* (Hilger, 1986).

13. P. Hamilton, M. Jaffe, J. M. Brown, L. Maisenbacher, B. Estey, and H. Müller, "Atom Interferometry in an Optical Cavity," Phys. Rev. Lett. **114**(10), 100405 (2015).

14. V. Xu, M. Jaffe, C. D. Panda, S. L. Kristensen, L. W. Clark, and H. Müller, "Probing gravity by holding atoms for 20 seconds," Science **366**(6466), 745–749 (2019).

15. C. P. Wang and R. L. Sandstrom, "Three-mirror stable resonator for high power and single-mode lasers," Appl. Opt. **14**(6), 1285–1289 (1975).

16. H. Carstens, S. Holzberger, J. Kaster, J. Weitenberg, V. Pervak, A. Apolonski, E. Fill, F. Krausz, and I. Pupeza, "Large-mode enhancement cavities," Opt. Express **21**(9), 11606 (2013).

17. A. Beyer, L. Maisenbacher, K. Khabarova, A. Matveev, R. Pohl, T. Udem, T. W. Hänsch, and N. Kolachevsky, "Precision spectroscopy of 2S–*n*P transitions in atomic hydrogen for a new determination of the Rydberg constant and the proton charge radius," Phys. Scr. **T165**, 014030 (2015).

18. Radiant Dyes MDI-H with Piezo Drive. Two Newport 8301-UHV Picomotor actuators have been added for coarse alignment.

19. Vacuum-compatible Nufern PM-S405-XP fiber in a 900 μm-diameter PEEK jacket, produced and AR-coated by Diamond GmbH.

20. Thorlabs MRF-polished diffraction-limited, high-precision aspheres AL1225H (stock item) and AL1225H-50URAD-SP (custom order, best possible surface quality with 50 μrad peak-valley slope, optimized for performance between 380-410nm).

21. J. Kruschwitz, "Technology boost in precision optics: The story of QED technologies inc," Optics and Photonics News **17**, 10–13 (2006).

22. S. N. Shafrir, H. J. Romanofsky, M. Skarlinski, M. Wang, C. Miao, S. Salzman, T. Chartier, J. Mici, J. C. Lambropoulos, R. Shen, H. Yang, and S. D. Jacobs, "Zirconia-coated carbonyl-iron-particle-based magnetorheological fluid for polishing optical glasses and ceramics," Appl. Opt. **48**(35), 6797 (2009).

23. C. Kumari and S. K. Chak, "A review on magnetically assisted abrasive finishing and their critical process parameters," Manuf. Rev. **5**, 13 (2018).

24. Bernhard Halle Nachfl. GmbH, Germany.

25. A. E. Siegman, "New developments in laser resonators," in *Optical Resonators*, vol. 1224 International Society for Optics and Photonics (SPIE, 1990), pp. 2–14.

26. C. Wang, X. Dun, Q. Fu, and W. Heidrich, "Ultra-high resolution coded wavefront sensor," Opt. Express **25**(12), 13736 (2017).

27. J.-C. Chanteloup, "Multiple-wave lateral shearing interferometry for wave-front sensing," Appl. Opt. **44**(9), 1559 (2005).

28. T. Ling, J. Jiang, R. Zhang, and Y. Yang, "Quadriwave lateral shearing interferometric microscopy with wideband sensitivity enhancement for quantitative phase imaging in real time," Sci. Rep. **7**(1), 9 (2017).

29. A. E. Siegman, *Lasers* (University Science Books, 1986).

30. ISO Standard 11146, "Lasers and laser-related equipment – Test methods for laser beam widths, divergence angles and beam propagation ratios," (2005).

31. H. W. N. Hodgson, *Laser Resonators and Beam Propagation. Fundamentals, Advanced Concepts and Applications* (Springer, 2005).

32. P. A. Bélanger, "Beam propagation and the ABCD ray matrices," Opt. Lett. **16**(4), 196–198 (1991).

33. A. E. Siegman, "Analysis of laser beam quality degradation caused by quartic phase aberrations," Appl. Opt. **32**(30), 5893 (1993).

34. J. Weitenberg, "Transversale Moden in optischen Resonatoren für Anwendungen hoher Laserintensität," Ph.D. thesis, RWTH Aachen (2017).

35. R. Paschotta, "Beam quality deterioration of lasers caused by intracavity beam distortions," Opt. Express **14**(13), 6069 (2006).

36. N. Bey, "Spektal aufgelöste Strahlqualitätsmessung," Master's thesis, RWTH Aachen (2013).

37. J. Weitenberg, P. Rußbüldt, I. Pupeza, T. Udem, H.-D. Hoffmann, and R. Poprawe, "Geometrical on-axis access to high-finesse resonators by quasi-imaging: a theoretical description," J. Opt. **17**(2), 025609 (2015).

38. B. Saleh and M. Teich, *Fundamentals of Photonics* (Wiley, 1991).

39. S. Amarande, A. Giesen, and H. Hügel, "Propagation analysis of self-convergent beam width and characterization of hard-edge diffracted beams," Appl. Opt. **39**(22), 3914 (2000).

40. Zemax OpticStudio 15.5, Professional Edition with Physical Optics Propagation (POP) option.

41. E. Brinkmeyer, "Backscattering in single-mode fibres," Electron. Lett. **16**(9), 329–330 (1980).

42. E. Brinkmeyer, "Analysis of the backscattering method for single-mode optical fibers," J. Opt. Soc. Am. **70**(8), 1010 (1980).

43. M. Nakazawa, "Rayleigh backscattering theory for single-mode optical fibers," J. Opt. Soc. Am. **73**(9), 1175 (1983).

44. D. Goldstein, *Polarized Light* (CRC, 2011).

45. R. Pohl, F. Nez, L. M. P. Fernandes, F. D. Amaro, F. Biraben, J. M. R. Cardoso, D. S. Covita, A. Dax, S. Dhawan, M. Diepold, A. Giesen, A. L. Gouvea, T. Graf, T. W. Hänsch, P. Indelicato, L. Julien, P. Knowles, F. Kottmann, E.-O. Le Bigot, Y.-W. Liu, J. A. M. Lopes, L. Ludhova, C. M. B. Monteiro, F. Mulhauser, T. Nebel, P. Rabinowitz, J. M. F. dos Santos, L. A. Schaller, K. Schuhmann, C. Schwob, D. Taqqu, J. F. C. A. Veloso, and A. Antognini, "Laser spectroscopy of muonic deuterium," Science **353**(6300), 669–673 (2016).

46. R. Pohl, F. Nez, T. Udem, A. Antognini, A. Beyer, H. Fleurbaey, A. Grinin, T. W. Hänsch, L. Julien, F. Kottmann, J. J. Krauth, L. Maisenbacher, A. Matveev, and F. Biraben, "Deuteron charge radius and Rydberg constant from spectroscopy data in atomic deuterium," Metrologia **54**(2), L1–L10 (2017).